



Spectroscopically unraveling high-valence Ni-Fe catalytic synergism in NiSe₂/FeSe₂ heterostructure

Shi Tao^a, Guikai Zhang^b, Bin Qian^a, Jun Yang^d, Shengqi Chu^{b,*}, Chencheng Sun^a, Dajun Wu^a, Wangsheng Chu^c, Li Song^{c,*}

^a School of Electronic and Information Engineering, Jiangsu Laboratory of Advanced Functional Materials, Changshu Institute of Technology, Changshu 215500, China

^b Beijing Synchrotron Radiation Facility, Institute of High Energy Physics Chinese Academy of Sciences, Beijing 100049, China

^c National Synchrotron Radiation Laboratory, University of Science and Technology of China, 230029, China

^d School of Material Science & Engineering, Jiangsu University of Science and Technology, 212003, China

ARTICLE INFO

Keywords:

Bimetallic selenides

Heterostructure

operando X-ray absorption spectroscopy

Surface reconstruction

Oxygen evolution reaction

ABSTRACT

Heterostructured compounds with rationally engineered interfaces are widely reported as efficient oxygen evolution reaction (OER) electrocatalysts, but the mechanism of the intrinsic activities still unclear. Herein, a typical model catalyst of NiSe₂/FeSe₂ heterostructure with a low overpotential of 230 mV at 10 mA cm⁻² and long-term durability is fabricated by selenizing Ni-Fe Prussian-blue analog (PBA) templates. *In-situ/operando* Raman spectroscopy and synchrotron-based X-ray absorption spectroscopy (XAS) are employed to reveal the real catalytic process. It is attested that the dynamic surface reconstruction into Ni-O-Fe configurations, and the high-valence Ni^{III}-O-Fe^{III} moieties in Ni-FeOOH is responsible for the high oxygen evolution. Density functional theory (DFT) simulations further confirm that the electron transfer driven by strong Ni-Fe synergistic effect in NiSe₂/FeSe₂ heterostructure not only improves the density of Ni/Fe active sites, but also modulates the nature active sites. This works may deepen our understanding of intrinsic activities of metal compound heterostructures and the correlation between dynamic surface structural evolution and catalytic activity.

1. Introduction

Developing sustainable and high-efficiency clean energy storage and conversion system is highly urgent for modern society, because of the increasing serious environmental problems. Electrochemical water splitting, fuel cells and metal-air batteries have been considered as promising approaches to accomplish sustainability future energy [1,2]. Oxygen evolution reaction (OER) as the anodic reaction in the above devices, which involves multiple proton-electron transfer steps, becomes the main bottleneck for practical application due to the sluggish kinetics [3–6]. More attention has been paid to search for low-cost, non-noble metal electrocatalysts with high-performance towards OER. Transition metal compounds (TMCs) with earth abundance and environmental green have been widely explored as potential catalysts for OER, such as oxides, sulfides, selenides, phosphides, layered double hydroxides and so on [7–14]. Among them, transition metal selenides (TMSs) with metallic conductivities thus attracted widespread concern, which are promising candidates to replace the noble metal oxides, such as IrO₂/RuO₂. However, the intrinsically poor activity and

unsatisfied stability greatly hinder their practical applications [15–20]. To date, extensive efforts have been devoted to improve their electrocatalytic activity by nanostructured optimization, cation/anion doping and multiple-phase combination. In particular, designing hybrid electrocatalysts with engineered interfaces in heterostructures has been regarded as an effective strategy to tune electronic structure and facilitate the reaction rate [21–24]. For example, unique Ni(CN)₂/NiSe₂ heterostructures, composed of single-crystalline Ni(CN)₂ nanoplates surrounded by crystallographically aligned NiSe₂ nanosatelites, exhibited superior enhanced electrocatalytic performance, benefitting from the optimized geometric and electronic structures [25]. NiSe₂/CoSe₂ heterostructure nanohybrid was synthesized by ion injection method and demonstrated outstanding performance for oxygen electrocatalysis due to the dense heterointerfaces [26]. Although TMSs-based heterogeneous catalysts have achieved much progress in nanoengineering, and surpassed the benchmark noble-metal (Ir or Ru-based) oxides, but their catalytic activity is still hindered by the synergy of different adsorbed intermediates. Therefore, identifying the intrinsic catalytically active sites on the catalysts' near-surface and

* Corresponding authors.

E-mail addresses: chusq@ihep.ac.cn (S. Chu), song2012@ustc.edu.cn (L. Song).

<https://doi.org/10.1016/j.apcatb.2023.122600>

Received 8 October 2022; Received in revised form 30 January 2023; Accepted 6 March 2023

Available online 11 March 2023

0926-3373/© 2023 Elsevier B.V. All rights reserved.

unveil the fundamental electrochemical mechanism during working operation is critical for rational design of effective electrocatalysts [27–30]. Key fundamental issues are still not elucidated so far. How does the heterogeneous interface work? What is the intermediate in the true catalyst? How do the intermediates affect the OER activity? An atomistic understanding of the oxygen generation process is a fundamental prerequisite for OER activity, due to the complicated atom-and charge-transfer process in typical heterostructured catalysts. These still need to be explained at the atomic scale, but also a great challenge due to the complexity of surface reconstruction and limited resolution of *operando* characterization techniques [31,32]. Therefore, developing a simple method to synthesize stable catalysts with heterostructures and elucidating the detailed electrocatalytic mechanism are important for expediting industrial upgrade. To conclude, systematic research is needed to identify atomic interface configurations under working condition with space-resolved and time-resolved techniques as well as their structure-activity correlation, which is extremely essential for designing efficient catalysts.

Herein, we report a facile strategy for synthesizing NiSe₂/FeSe₂ heterostructure coupled with N-doped carbon (NiSe₂/FeSe₂-NC) hybrid composites via in situ selenizing bimetallic Ni-Fe PBA precursor. The as-fabricated NiSe₂/FeSe₂-NC as OER electrocatalyst displays remarkable performance, achieving the low overpotential of 230 mV at 10 mA cm⁻² and long-term durability under alkaline condition. The outstanding catalytic property is ascribed to the modulation of geometric structure and high heterostructure interface between the NiSe₂ and FeSe₂ nano-hybrid. Combining *In-situ/operando* Raman spectroscopy and X-ray absorption spectroscopy (XAS) investigate intrinsic catalytically active sites at atomic scale and confirm that the NiSe₂/FeSe₂-NC exhibits obvious surface reconstruction with Ni/Fe oxyhydroxides, and the high-valence Ni^{III}-O-Fe^{III} moieties acts as the real activity for OER. Particularly, the synergistic mechanism of the heterogeneous components has been disclosed on interfacial reaction intermediates. Our finding offers the fundamental catalytic mechanism of heterostructural electrocatalyst for optimizing structural design advanced catalysts.

2. Experimental section

2.1. Chemicals

Ni(CH₃COO)₂·4 H₂O, Na₃C₆H₅O₇·2 H₂O, K₃[Fe(CN)₆]·6 H₂O, K₄[Fe(CN)₆]·3 H₂O, ethanol and Se powder were purchased from Sinopharm Chemical Reagent Shanghai Co. Polyvinyl pyrrolidone (K30) purchased from Beijing Voke Biotechnology Co. LTD. RuO₂ powder was bought from Sigma-Aldrich (USA).

2.2. Synthesis of Ni-Fe PBA precursors

1.2 mmol Ni(CH₃COO)₂·4H₂O and 1.5 mmol Na₃C₆H₅O₇·2H₂O were dissolved into 60 mL deionized water forming solution A. 1.2 mmol K₃[Fe(CN)₆]·6 H₂O was dissolved into 40 mL deionized water forming solution B, then was dropped into solution A. The above mixed solution under continuous stirring for 30 min and then rested overnight. The precipitate was centrifuged and washed with deionized water three times. The obtained yellow powder were collected and vacuum dried at 80 °C for overnight.

2.3. Synthesis of NiSe₂/FeSe₂-NC hybrid composites

The 100 mg Ni-Fe PBA precursors and 1 g Se powder were placed at the bottom and upstream of corundum boat, respectively. Then, the corundum boat was sealed in tube furnace and annealed at 500 °C for 2 h under Ar/H₂ (v/v=95/5) atmosphere with a heating rate of 5 °C min⁻¹. After cooling naturally to room temperature, the final black powder was obtained. For comparison, the FeSe₂-NC and NiSe₂-NC were synthesized by the previous reports.

2.4. Synthesis of NiSe₂-NC and FeSe₂-NC standard sample

The NiSe₂-NC and FeSe₂-NC samples are fabricated by the similar method based on the previous works [33,34]. In details, Polyvinyl pyrrolidone (250 mg) and Ni(CH₃COO)₂·4 H₂O (249 mg) were dispersed in 30 mL ethanol under ultrasonication to get a homogenous solution, which was then transferred into a sealed Teflon-lined autoclave (50 mL) at 120 °C for 6 h. After the autoclave was cooled down to room temperature, the precipitate was collected and washed several times with ethanol to obtain the Ni-based acetate hydroxide. The 50 mg as-prepared Ni-based acetate hydroxides as precursor and 250 mg Se powder were at the bottom and upstream of corundum boat, respectively. The pyrolysis was performed in N₂ atmosphere at 500 °C for 2 h with a ramp of 2 °C min⁻¹. For FeSe₂-NC sample, 110 mg K₄Fe(CN)₆·3 H₂O and 2 g polyvinyl pyrrolidone (PVP) were added into the above solution. The mixture was stirred for 1 h, and then the suspensions were transferred into a Teflon-lined stainless steel autoclave (100 mL) to react under the temperature of 80 °C for 24 h. A precipitate was collected and washed with deionized water and ethanol for several times. The precursors were obtained after vacuum drying at 60 °C for overnight. The as-prepared precursors were placed at the downstream side of corundum boat and 2 g Se powder was located at the upstream side in the tube furnace. Then, the furnace was heated to 500 °C with a heating rate of 2 °C min⁻¹ under Ar/H₂ (95/5, v/v) flow for 2 h.

2.5. Characterization

The X-ray powder diffraction (XRD) patterns were recorded by a Bruker D8 ADVANCE X-ray diffractometer with Cu Kα radiation (λ = 0.15418 nm) at a scanning rate of 4° min⁻¹. Field-emission scanning electron microscopy (SEM) images were obtained on a ZEISS microscope with an accelerating voltage of 20 kV. Transmission electron microscopy (TEM) images and high-resolution TEM (HRTEM) images were obtained by a JEOL JEM-2000CX instrument. Nitrogen adsorption and desorption isotherm was characterized by a ASAP2020. The X-ray photoelectron spectroscopy (XPS) experiments were carried out on a PHI-5400 electron spectrometer. The Raman spectrum was performed by a Raman spectrometer (Horiba Xplora). The Ni, Fe K-edge X-ray absorption spectroscopy (XAS) was collected from the 1W1B beamline of Beijing Synchrotron Radiation Facility (BSRF). Ni, Fe L-edge, C and N K-edge XAS spectroscopy was tested from the 4B7B beamline of BSRF.

2.6. Electrochemical measurements

In brief, the catalyst (4 mg) was dispersed in a water/isopropanol solution (1 mL, 3:1 v/v) with 30 μL Nafion solution (Sigma Aldrich, 5 wt %) by sonicating for 40 min to form a homogeneous ink. Then, 15 μL of dispersion was loaded onto a glassy carbon electrode with a diameter of 5 mm (loading ~0.36 mg cm⁻²). Finally, the as-prepared catalyst film was dried at room temperature. The OER activity of catalysts was measured in a three-electrode glass cell filled with O₂-saturated 1.0 M KOH electrolytes on an electrochemical workstation CHI660E (Chenhua, China) using a KCl-saturated Ag/AgCl electrode as the reference electrode, a Pt wire as the counter electrode and the electrocatalyst-loaded glassy carbon as the working electrode. Note that the current density was normalized to the geometrical area and the measured potentials vs Ag/AgCl were converted to a reversible hydrogen electrode (RHE) scale according to the Nernst equation ($E_{\text{RHE}} = E_{\text{Ag/AgCl}} + 0.059 \text{ pH} + 0.197$); the overpotential (η) was calculated according to the following formula: $\eta(\text{V}) = E_{\text{RHE}} - 1.23 \text{ V}$. Polarization curves for OER activities were obtained by linear sweep voltammetry with a scan rate of 5 mV s⁻¹, respectively. Electrochemical impedance spectroscopy (EIS) dates were recorded with frequency range of 0.1–100 kHz at a bias potential of 1.55 V (vs. RHE) for OER. Cyclic voltammetry (CV) was conducted to probe the double-layer capacitor (*C_{dl}*) to calculate the electrochemically active surface area (ECSA).

2.7. DFT calculations

Density functional theory (DFT) calculations were performed by using the Vienna ab initio Simulation Package (VASP) with the projector augmented wave (PAW) method [35,36]. The Perdew-Burke-Ernzerh (PBE) functional was used within the Generalized Gradient Approximation (GGA) for exchange correlation energy [37]. The electronic wave functions were expanded in a plane wave basis set with an energy

cutoff of 450 eV. The electron states were sampled using a k-point mesh of Γ -centered. To calculate the electronic properties and catalytic activity of the NiSe₂/FeSe₂ catalyst, the pristine and oxidized (111) slab surface model of the NiSe₂/FeSe₂ heterostructure were used. In addition, the activity edge of Ni(OH)₂ (Fe(OH)₂) nanolayer was calculation to further simulated the effect of Fe-O-Ni. Structural optimizations were performed by minimizing the forces on all atoms to be below 0.02 eV·Å⁻¹ and the self-consistent calculation energy to be below 10⁻⁶ eV.

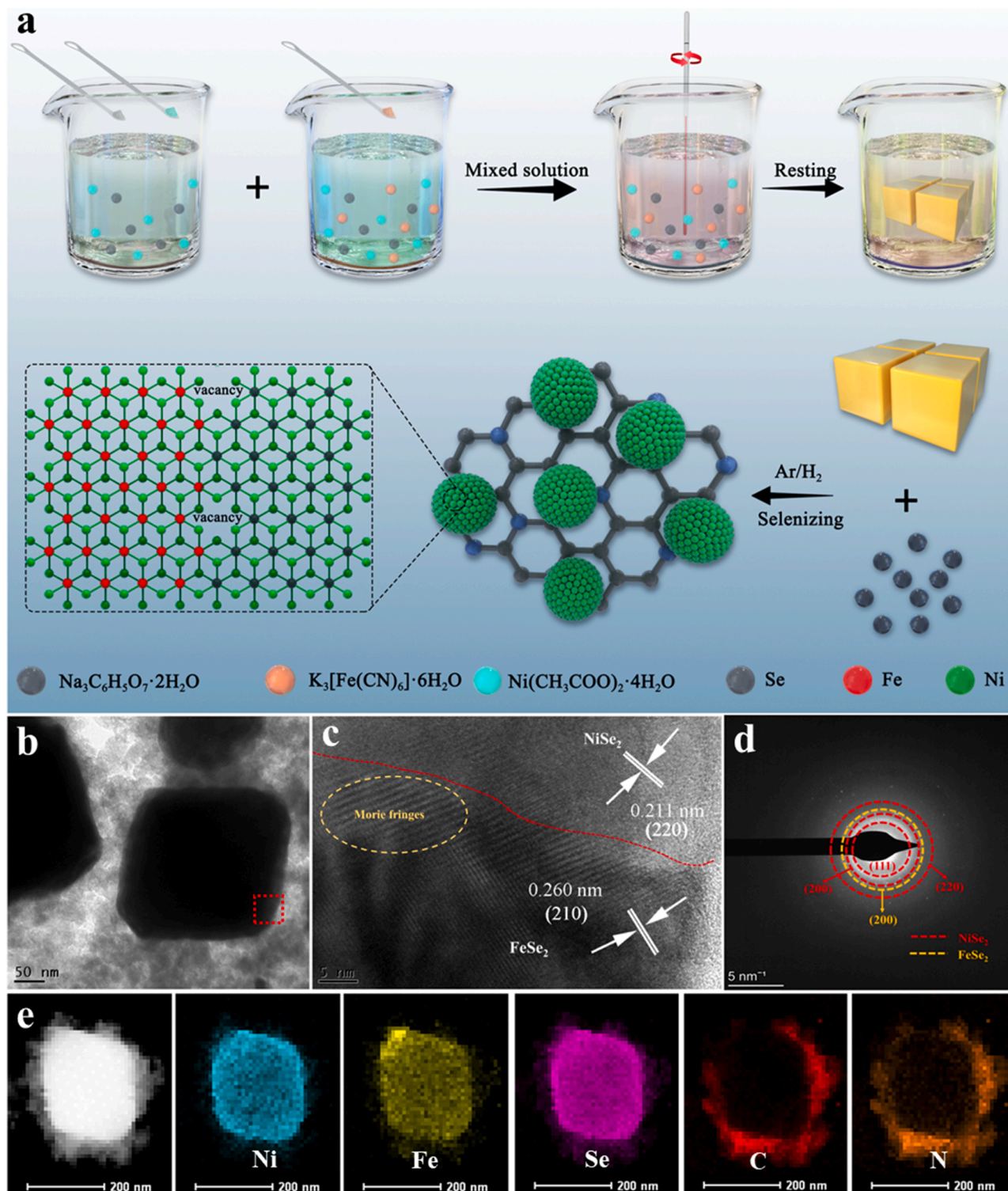


Fig. 1. Fabrication and characterization of NiSe₂/FeSe₂-NC heterostructure. (a) Schematic of the preparation process. (b) TEM images and (c) high-resolution TEM image of NiSe₂/FeSe₂-NC. (d) The corresponding SAED pattern. (e) Elemental mapping images.

3. Results and discussion

3.1. Compositional synthesis and analysis

Fig. 1a presents schematically the synthesis procedure of $\text{NiSe}_2/\text{FeSe}_2\text{-NC}$ composite. The bimetallic Ni-Fe PBA was used as precursor. It is a yellow powder that displays plenty of regular cubes with the size of about $1.0\ \mu\text{m}$ in SEM images (Fig. S1), and the XRD pattern is in line with the nickel iron cyanide hydrate phase $\text{Ni}(\text{Fe}(\text{CN})_6)_{0.667}(\text{H}_2\text{O})_{3.333}$ (PDF# No. 86-0501), a typical PBA material. EDX spectrum confirms the Ni/Fe ratio of about 1:0.74 in the precursor (Fig. S2). Then the resulting bimetallic selenide composite $\text{NiSe}_2/\text{FeSe}_2\text{-NC}$ was obtained via selenizing the precursors in Ar/H_2 atmosphere at $500\ ^\circ\text{C}$, and meanwhile, Prussian blue framework was pyrolyzed in situ into N-doped carbon (NC). A large number of microspheres with rough surfaces are observed from SEM images in the end product (Fig. S3), not retaining the cubic shape as the precursor. The XRD pattern (Fig. S4a) reveals two separate phases in $\text{NiSe}_2/\text{FeSe}_2\text{-NC}$, the pyrite-type cubic NiSe_2 (PDF # 41-1495) and FeSe_2 (PDF # 48-1881), indicating the formation of heterostructure. The element ratio of Ni, Fe in $\text{NiSe}_2/\text{FeSe}_2\text{-NC}$ is around 1:0.67, close to the Ni/Fe ratio of the precursor (Fig. S4b). Further TEM

images in Fig. 1b and Fig. S5 show $\text{NiSe}_2/\text{FeSe}_2$ cuboids tightly supported on the NC, the microstructure morphology of heterostructured $\text{NiSe}_2/\text{FeSe}_2\text{-NC}$ was further characterized by high-resolution TEM in Fig. 1c, showing the atomically intimate contact between NiSe_2 and FeSe_2 supporting on NC with clear lattice spacing of 0.211 and 0.260 nm, corresponding to the (220) plane of NiSe_2 and (210) plane of FeSe_2 , respectively. The related SAED pattern shown in Fig. 1d illustrates the semicoherent phase boundary of NiSe_2 and FeSe_2 in detail, and provides a deep insight into the heterostructure. The interface length is typically around 20 nm and the elemental mapping in Fig. 1e shows Ni, Fe, Se, C and N are homogeneously dispersed in the $\text{NiSe}_2/\text{FeSe}_2\text{-NC}$. As previously reported, the abundant heterogeneous nanointerfaces are expected to provide favorable charge transfer between the core selenides and surface, thereby enhancing the synergistic activity of electrocatalyst [38,39].

The chemical state and atomic structure of heterostructured $\text{NiSe}_2/\text{FeSe}_2\text{-NC}$ composite were explored by XPS and synchrotron XAFS. To better elucidate the interaction of bimetallic sites, the relevant monometallic selenides with similar features, such as $\text{NiSe}_2\text{-NC}$ and $\text{FeSe}_2\text{-NC}$, have been prepared for comparison. The XPS survey for $\text{NiSe}_2/\text{FeSe}_2\text{-NC}$ (Fig. S6) indicates the presence of Ni, Fe, Se, C and N. Firstly,

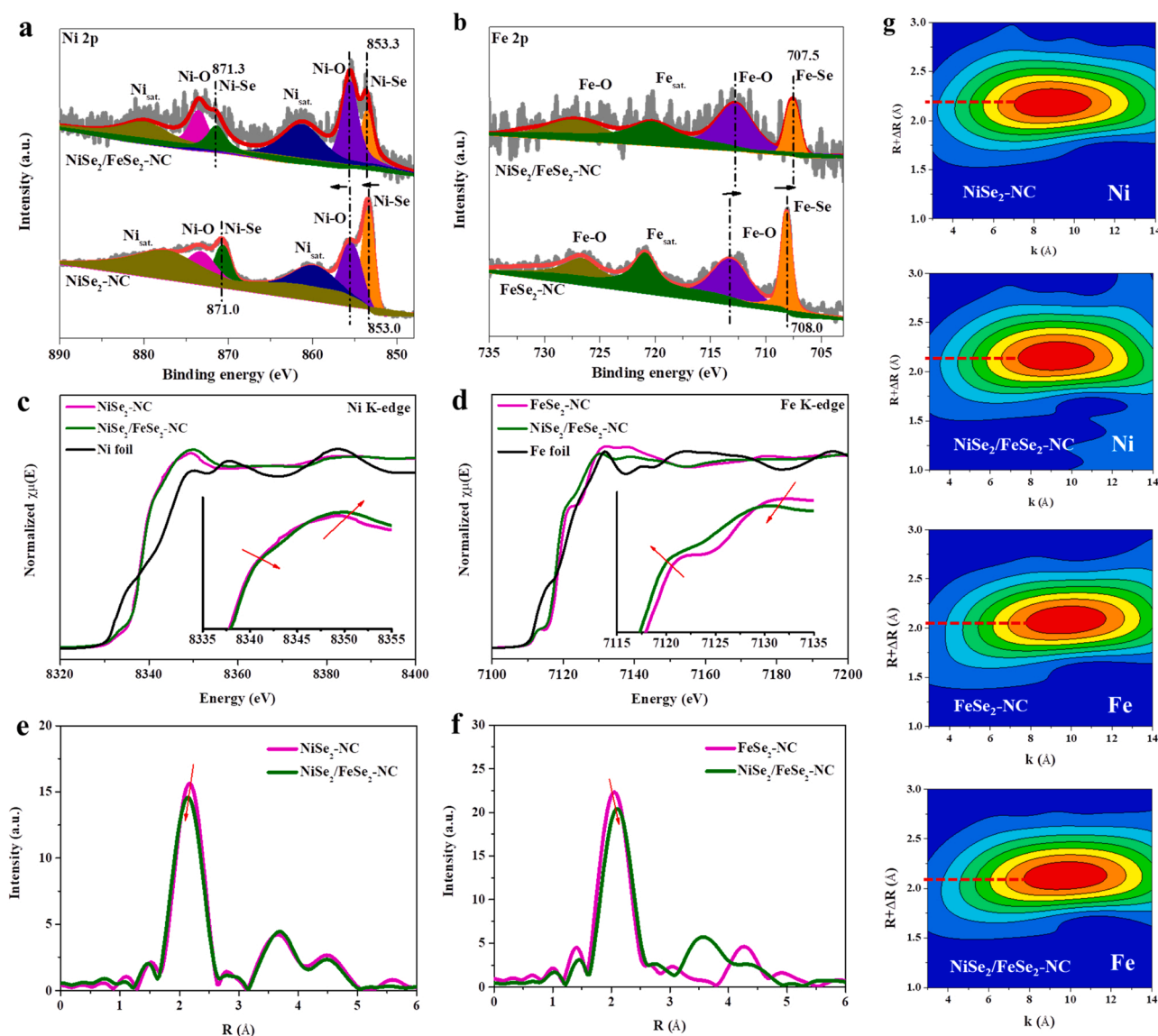


Fig. 2. X-ray spectroscopy analysis of $\text{NiSe}_2/\text{FeSe}_2\text{-NC}$. High-resolution XPS spectra for (a) Ni 2p, (b) Fe 2p. (c) Normalized Ni K-edge and (d) Fe K-edge XANES spectra. FT-EXAFS curves of (e) Ni and (f) Fe. (g) Wavelet transform for the k^3 -weight EXAFS for Ni and Fe K edges.

on the high resolution XPS spectra, the Ni 2p_{3/2} peaks shift positively about 0.3 eV (Fig. 2a) and Fe 2p_{3/2} peaks shift negatively about 0.5 eV (Fig. 2b) in NiSe₂/FeSe₂-NC as compared with the corresponding single phases, indicating the existence of high-valence Ni and low-valence Fe in the heterostructure [40]. In monometallic selenides, the formal valence of Ni/Fe metal sites is mainly +2, as seen by the high resolution XPS spectra in Figs. 2a and 2b. For Se 3d XPS spectrum in Fig. S7, the fitted two peaks at 55.3 and 56.3 eV are corresponding to Se 3d_{5/2} and Se 3d_{3/2} of Se₂²⁻ in the NiSe₂/FeSe₂-NC, which exhibits red-shift compared to the NiSe₂-NC and FeSe₂-NC [41]. These results strongly suggest the strong electronic interactions between NiSe₂ and FeSe₂ nanodomains, demonstrating the construction of heterostructure interfaces. The high-resolution of C and N 1s spectrum for NiSe₂/FeSe₂-NC, NiSe₂-NC and FeSe₂-NC (Fig. S8) can confirm that the formation of N-doped carbon, which enhance both the reaction kinetics and electrical conductivity of the entire electrode, thereby contributing to the fast electron transfer of electrocatalysts and the robust durability [42,43].

X-ray absorption near-edge structure (XANES) spectroscopy analyses are performed to identify the valence state of atoms. As further confirmed by XANES spectra, the absorption edge of Ni K-edge in as-

prepared NiSe₂/FeSe₂-NC shifts slightly to a higher energy relative to NiSe₂-NC (Fig. 2c), whereas Fe edge shifts to the lower energy relative to FeSe₂-NC (Fig. 2d), coinciding with aforementioned XPS results and indicating the electron transfer from Ni to Fe. This phenomenon could be attributed to the built-in electric field where electrons transferred from the NiSe₂ domains to FeSe₂, triggering the redistribution of interfacial charge and yielding more positively charged Ni in NiSe₂/FeSe₂-NC. As reported widely by prior theoretical and experimental results, high-valence Ni will reduce the energy barriers and achieve high catalytic activity for oxygen generation [44]. It is also noteworthy that the Fe oxidation state decreases and its change is larger than Ni sites, which could have a profound effect on the catalytic behaviour of Fe. Secondly, the Fourier transformed EXAFS spectra manifest a strained lattice with shorter Ni-Se bond and larger Fe-Se bond in NiSe₂/FeSe₂-NC comparing with the single phases, as shown in Fig. 2e & f and fitting results in Fig. S9. According to the change of valence states and bond distances, the stronger Ni-Se bonding and weaker Fe-Se bonding should coexist in NiSe₂/FeSe₂-NC. The wavelet transform (WT) simulations were employed to further provide a visualized structural disorder and radial distance resolution in k space (Fig. 2g). This strained lattice is supposed

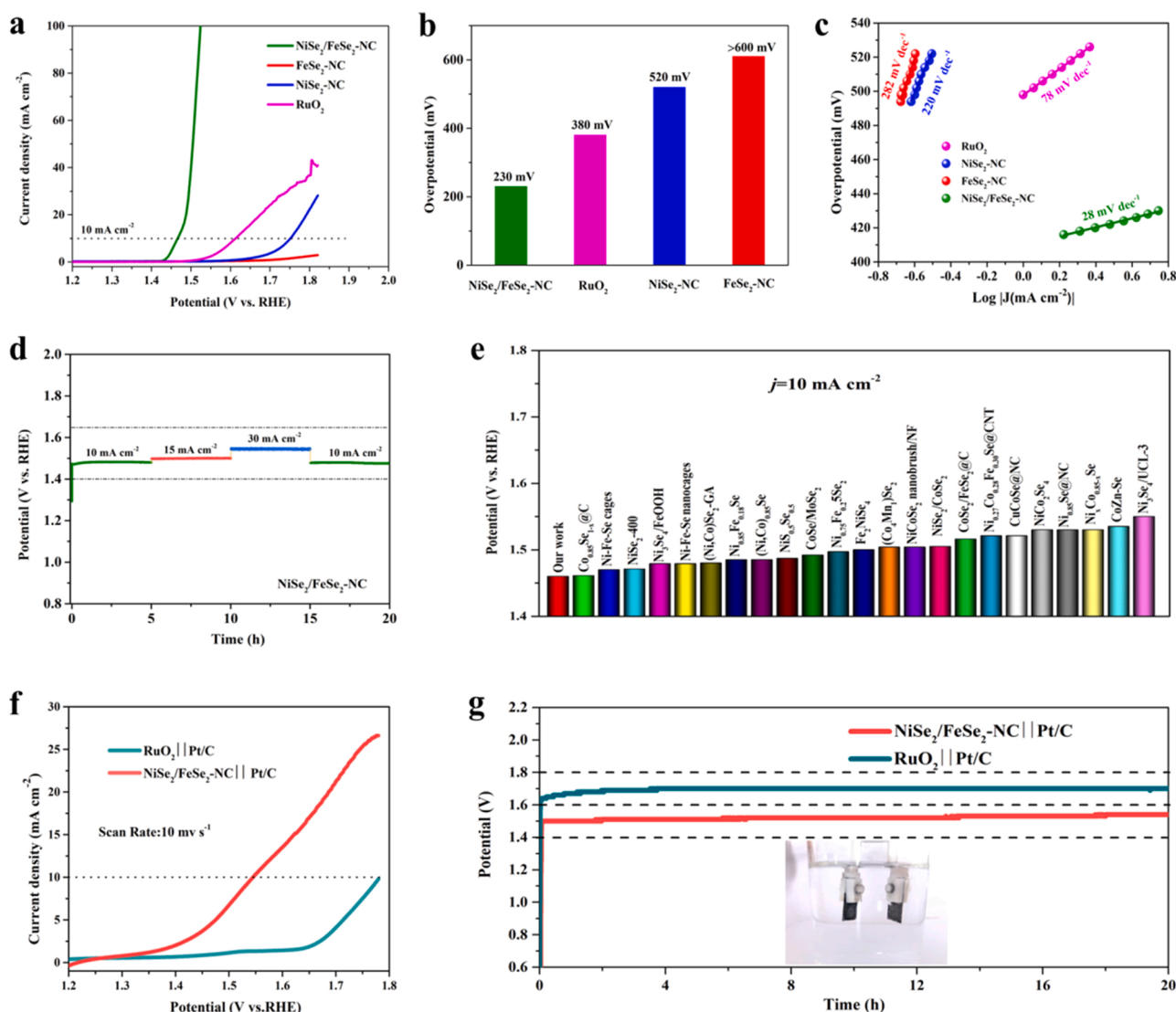


Fig. 3. OER activity evaluation. (a) IR-corrected polarization LSV curves at 5 mV s⁻¹. (b) Comparison of overpotentials at j = 10 mA cm⁻² for different catalysts. (c) Corresponding Tafel plots. (d) Long-term stability test at different current densities. (e) Comparison of the overpotential at 10 mA cm⁻² for NiSe₂/FeSe₂-NC with the previously reported metal selenide catalysts. (f) Polarization curves for NiSe₂/FeSe₂-NC || Pt/C and RuO₂ || Pt/C devices for overall water splitting. (g) Chronopotentiometric measurements of stability at 10 mA cm⁻² (Inset is the digital photograph of NiSe₂/FeSe₂-NC || Pt/C water-splitting device).

to be induced by the strong synergistic effect between Ni and Fe atoms, which may also play a critical role in accelerating the OER reaction kinetic. Meanwhile, as evidenced by EPR experiments (Fig. S10), a large number of Se vacancies are embedded in heterostructured NiSe₂/FeSe₂-NC, and the unsaturated Se coordination shell around transition metals is also verified by the decreasing coordination numbers of both the Ni/Fe-Se bond in EXAFS spectra (Table S1) [45]. All the above results demonstrate that our synthesized NiSe₂/FeSe₂-NC heterostructure is endowed with tuned electronic structure and strained lattice, along with abundant interfaces and numerous vacancies, which will enhance the OER performance by augmenting the Ni-Fe synergistic effect and providing more exposed active sites.

3.2. Catalytic performance

The OER catalytic performances of as-prepared composites are tested using common three-electrode setup in 1 M KOH solution. Fig. 3a shows the linear sweep voltammetry (LSV) polarization curves that NiSe₂/FeSe₂-NC exhibits best catalytic activity compared with RuO₂, NiSe₂-NC and FeSe₂-NC. The overpotential of NiSe₂/FeSe₂-NC is only 230 mV at 10 mA cm⁻², which is lower than RuO₂ (380 mV), NiSe₂-NC (520 mV) and FeSe₂-NC (>600 mV) in Fig. 3b. Additionally, the FeSe₂-NC displays poor catalytic activity. Tafel slopes of NiSe₂/FeSe₂-NC, RuO₂, NiSe₂-NC and FeSe₂-NC (Fig. 3c) are 28, 78, 220 and 282 mV dec⁻¹, respectively, indicating that NiSe₂/FeSe₂-NC is most efficient kinetics. The electrochemically active surface area (ECSA) of as-prepared samples is calculated by the double layer capacitances (C_{dl}), which can be obtained from cyclic voltammetry (CV) curves (Fig. S11, Supporting Information). The NiSe₂/FeSe₂-NC exhibits a higher C_{dl} of 0.56 mF cm⁻², than those of NiSe₂-NC (0.20 mF cm⁻²) and FeSe₂-NC (0.13 mF cm⁻²), implying that more exposed active sites in the heterostructural NiSe₂/FeSe₂-NC. Moreover, the Nyquist plots are provided in Fig. S12, further confirm this result with the lowest charge transfer resistance of (R_{ct} = 30.91 Ω) for NiSe₂/FeSe₂-NC among the other samples (Table S2), suggesting superior charge transfer ability due to the constructed heterostructure interfaces [46–48]. The chronopotentiometric (CP) test of NiSe₂/FeSe₂-NC at 10, 15, 30 and 10 mA cm⁻² sequentially for 20 h demonstrates catalytic durability (Fig. 3d). Compared to the previous metal selenide catalysts at 10 mA cm⁻² in Fig. 3e, the as-prepared NiSe₂/FeSe₂-NC shows that superior catalytic activity. Next, the electrocatalytic overall water splitting performance is evaluated by assembling with NiSe₂/FeSe₂-NC as cathode and Pt/C as anode. For comparison, the commercial RuO₂ powder is also tested under the same conditions as the cathode. Fig. 3f displays comparison of the LSV curves of NiSe₂/FeSe₂-NC = |Pt/C and RuO₂||Pt/C, which illustrates that the electrocatalytic activity of NiSe₂/FeSe₂-NC = |Pt/C is better than RuO₂||Pt/C. Moreover, the catalytic stability of NiSe₂/FeSe₂-NC = |Pt/C and RuO₂||Pt/C is shown in Fig. 3g at 10 mA cm⁻², and the curve is stable for 20 h without obvious decaying. Notably, gas bubbles could be clearly observed at the surface of both electrodes by applying the oxidized potential. With regard to the operating stability as important metric, the as-prepared NiSe₂/FeSe₂-NC could be served as promising industrial candidate for overall water splitting.

Given the electrochemical stability of NiSe₂/FeSe₂-NC during OER process, we further investigate the microstructural change after stability test by using TEM, XPS and soft XAS. The TEM images confirm the microstructure of microspheres supported on NC for NiSe₂/FeSe₂-NC is well maintained after OER durability test. Obviously, it is observed that an amorphous layer with around 20 nm forms on the surface of NiSe₂/FeSe₂-NC (Fig. S13), suggesting the formation of Ni/Fe oxides/hydroxides. EDX mapping images suggest that homogeneous distribution of Ni, Fe, Se, N, C and O (over-oxidized) in NiSe₂/FeSe₂-NC, accompanying with Se leached from the surface, which could be further supported by ICP-AES test that there was Se but no Ni and Fe in the KOH electrolyte (Table S3).

XPS and soft X-ray XAS results of the post-catalyst after OER test for

10 h, show the high-valence Fe exists. The Ni (Fe) 2p spectra of NiSe₂/FeSe₂-NC before and after OER test displays that disappearance of Ni (Fe)-Se bonds and increasing Ni-O phase suggest that the NiSe₂/FeSe₂-NC catalyst was oxidized into Ni/Fe oxides/hydroxides species (Fig. S14 and S15) [49]. Meanwhile, the absence of Se 3d spectrum after OER in Fig. S16 suggests that the evolved surface structure (NiOOH/FeOOH). From Ni and Fe L-edge XAS spectra, which derive from the 2p to the unoccupied 3d orbital of dipole transitions. Ni and Fe L₃-edge region are featured by two main peaks due to the crystal field splitting effect, which can be assigned to Ni/Fe 3d t_{2g} and 3d e_g, (Fig. S17 and 18) [26]. The oxidation states of Ni/Fe element can be identified according to the references samples, Ni²⁺/Fe²⁺ cations in NiSe₂/FeSe₂-NC were partially oxidized into Ni³⁺/Fe³⁺ with two feature peaks located at 854.9/706.2 eV, implying the enhanced oxidation state of both Ni and Fe sites [50,51]. Additionally, the O K-edge spectra was collected and shown in Fig. S19. The local intensity maxima between 528 and 535 eV corresponding to the transition of the O 2p electron into the lowest unoccupied t_{2g} and e_g orbitals of Ni/Fe 3d band for before OER sample [52]. As compared with Ni(OH)₂ reference, the pre-edge peak at 533.0 eV is attributed to the hydroxy species (OH) [53]. After OER test, the peak at 533.0 eV increases significantly, demonstrating the formation of Ni/Fe hydroxides [54], which are referred to as the important products during OER. Based on the above results, confirming a dynamically evolved surface structure composed of NiOOH/FeOOH with NiSe₂/FeSe₂ as the core after OER.

3.3. Intrinsic OER mechanism

With the aim of revealing the surface evolution of NiSe₂/FeSe₂-NC electrocatalyst during the OER reaction, *In situ* Raman spectroscopy was employed to explore the intermediate species (Fig. 4a). As shown in Fig. 4b, the Raman intensity mapping was collected at the potential range of 1.1–1.8 V. With the potential increasing, two peaks at 475 and 556 cm⁻¹ appear and become stronger, which can be attributed to the A_{1g} stretching vibration mode of Ni^{III}-O in NiOOH, respectively [55]. Similarly, a weak vibration peak can be observed at about 720 cm⁻¹ is assigned to Fe-O bonds, indicating that the oxidation of Ni and Fe in NiSe₂/FeSe₂-NC. The peaks at 800–850 cm⁻¹ can be assigned to selenite (SeO₃²⁻) and selenate (SeO₄²⁻) [56]. On the NiSe₂/FeSe₂-NC surface, the bridge-mode O-O⁻ at about 1145 cm⁻¹ displays an increase signal from 1.2 to 1.8 V, proposing that the active O-O⁻ intermediate formation [57]. Therefore, it can be seen that the both NiSe₂ and FeSe₂ domains are the catalytic sites in the NiSe₂/FeSe₂-NC. We also performed the isotopic control Raman test using NiSe₂-NC and FeSe₂-NC samples to explore the function of Ni and Fe. As shown in Fig. 4c and d, there was no O-O⁻ species signal for NiSe₂-NC with the potential increasing, strong Ni^{III}-O bond was observed. In contrast, the O-O⁻ appear and no Fe-O species for FeSe₂-NC, indicating that Fe atoms have superior O-O⁻ adsorption compare with Ni atoms [58]. Therefore, we propose that the FeSe₂ nanodomains are the adsorption sites for OH⁻ ions and catalyze the O-O⁻ intermediate formation in heterostructural NiSe₂/FeSe₂-NC, while NiSe₂ can transform the O-O⁻ intermediate to final O₂ product.

Operando XAFS measurements have been conducted to further uncover the structure-activity relationship during the OER catalysis in alkaline electrolytes (Fig. S20). As shown in Fig. 5, the Ni and Fe K edges XAFS data of NiSe₂/FeSe₂-NC sample were collected with the applied potential up to 1.8 V vs. RHE. The obvious up-shifting of both the absorption edges and white line intensities indicates the increasing trend of valence states on Ni and also Fe sites (Figs. 5a and 5b). In the Fourier-transformed EXAFS spectra, the first shell at ca. 2.1 Å, which attributes to Ni/Fe-Se bonds, are decreasing caused by the Se species dissolution (Figs. 5c and 5d). These results undoubtedly confirm the *in situ* reconstruction of both Ni and Fe with the applied potentials, which could form the real dual active centers to significantly boost the OER performance.

The activity of Ni species is widely verified in various Ni-Fe-based

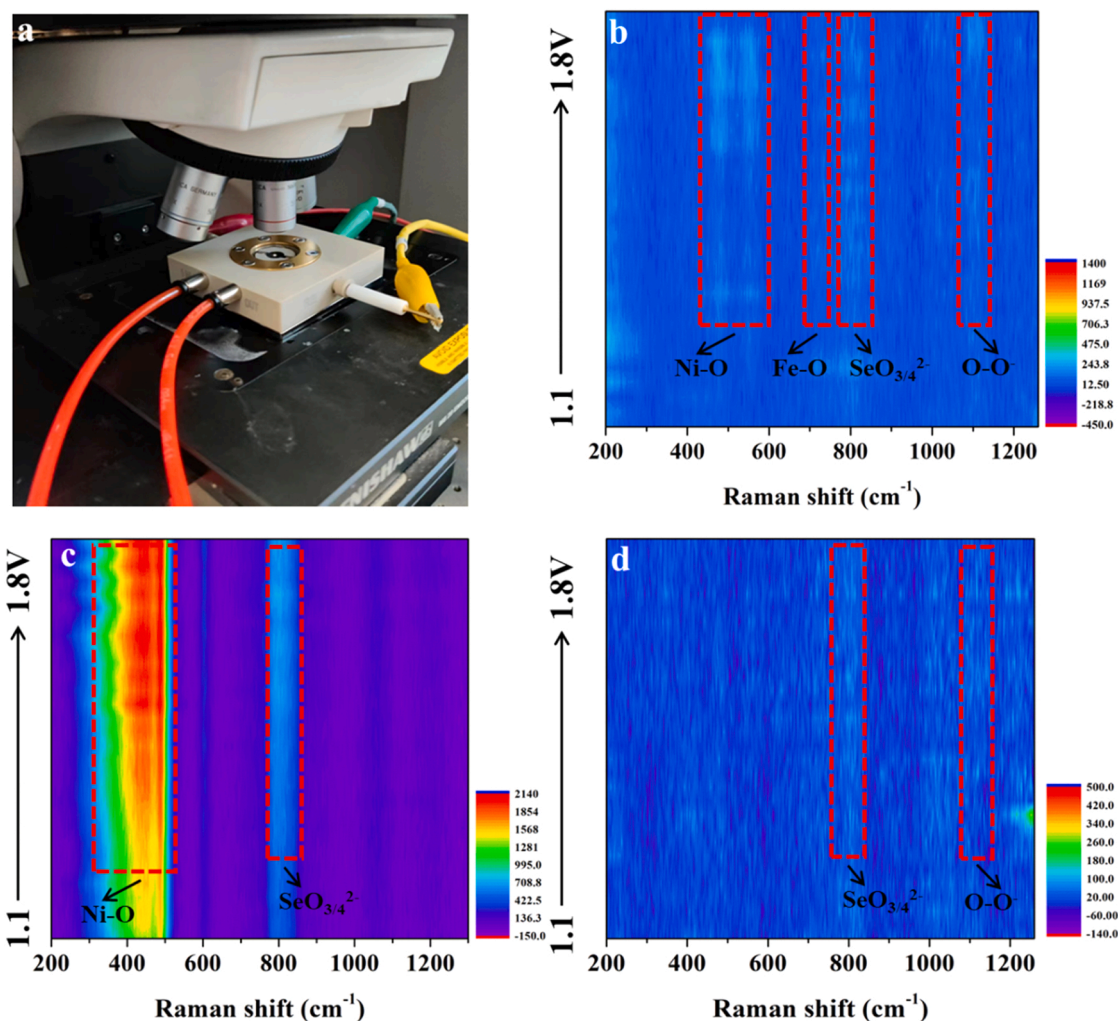


Fig. 4. *In-situ* Raman characterization during the OER process. (a) Photo of the testing process. Raman intensity mappings of (b) NiSe₂/FeSe₂-NC, (c) NiSe₂-NC, and (d) FeSe₂-NC catalysts as a function of applied potential.

OER electrocatalysts, but the role of Fe is still under long-time debate. Some recent works find that Fe is just for optimizing the electronic structure of Ni species. To further reveal the role of Fe in our synthesized bimetallic selenides NiSe₂/FeSe₂-NC, we compare the structural changes of several catalysts under *in situ* OER process. From the *operando* XAFS measurements with the applied potential, the NiSe₂-NC undergoes an evident structural transformation into (oxy)hydroxides during OER process, whereas the FeSe₂-NC stays almost unchanged (Fig. S21, S22 and Table S4). However, both of them are proven to have a poor OER activity based on the aforementioned LSV curves.

In addition, difference EXAFS (Diff-EXAFS) method is employed to reveal the local structure with a high accuracy [59]. The Diff-EXAFS spectra of Fe atoms in NiSe₂/FeSe₂-NC are obtained by subtracting the normalized XAFS spectrum at OCV from the ones at various potentials during OER process, which are denoted as diff_1.1 V-OCV and so on (Fig. S23). From the Fourier-transformed Diff-EXAFS spectra (Fig. 5e), three main peaks are observed to increase with the applied potentials, representing coordination shells of Fe-O at about 1.6 Å, Fe-Se at 2.1 Å, and Fe-M (M denotes Ni/Fe) at 2.7 Å, respectively. This means the raise of Fe oxidation state as well as the loss of Se atoms (as the magnitude of Fe-Se shell are negative in the difference spectra). It is noted that the Fe-M shell appears at above 1.4 V and gradually increases, which is not found in the monometallic catalyst FeSe₂-NC. Considering that the O-bridged heteroatom coordination may be an important factor in the enhancement of OER activity [60], we suggest the Fe-M can be

attributed to O-bridged Fe-Ni coordination structure (Ni^{III}-O-Fe^{III}), and it is well confirmed by the quantitative fitting results of diff_1.8 V-OCV (Fig. 5f and Table S5). This post-formed Ni^{III}-O-Fe^{III} structure at the surface may serve as the real active centers for OER in heterostructured NiSe₂/FeSe₂-NC.

3.4. Theoretical insights

Furthermore, density functional theory (DFT) calculations are used to elucidate the underlying mechanism of the high activity in NiSe₂/FeSe₂-NC. Differential charge density of NiSe₂/FeSe₂ heterostructure shows that the electron density significantly accumulates near the Fe sites (Fig. 6a), indicating the migration of electrons from NiSe₂ to FeSe₂ on the interface, as also evidenced by aforementioned XPS and XANES results (Fig. 2). According to the density of state (DOS) calculations, the electron density of NiSe₂/FeSe₂-NC is higher than monometallic NiSe₂ at the Fermi level and dominated by the Fe 3d orbitals (Fig. 6b and S24). This result suggests that the electron conductivity is improved by fabricated with NiSe₂/FeSe₂ heterointerface, helping to enhance the charge transfer rate and subsequent OER reaction kinetics [61]. Meanwhile, the formation energy of Se vacancy has been calculated. As shown in Fig. 6c, for monometallic selenides, the Se atoms in NiSe₂ are easy to dissolve, while more difficult in FeSe₂, which are consistent with our *operando* observations. And in NiSe₂/FeSe₂-NC, it just lies between them. We think this intermediate formation energy of Se vacancy would

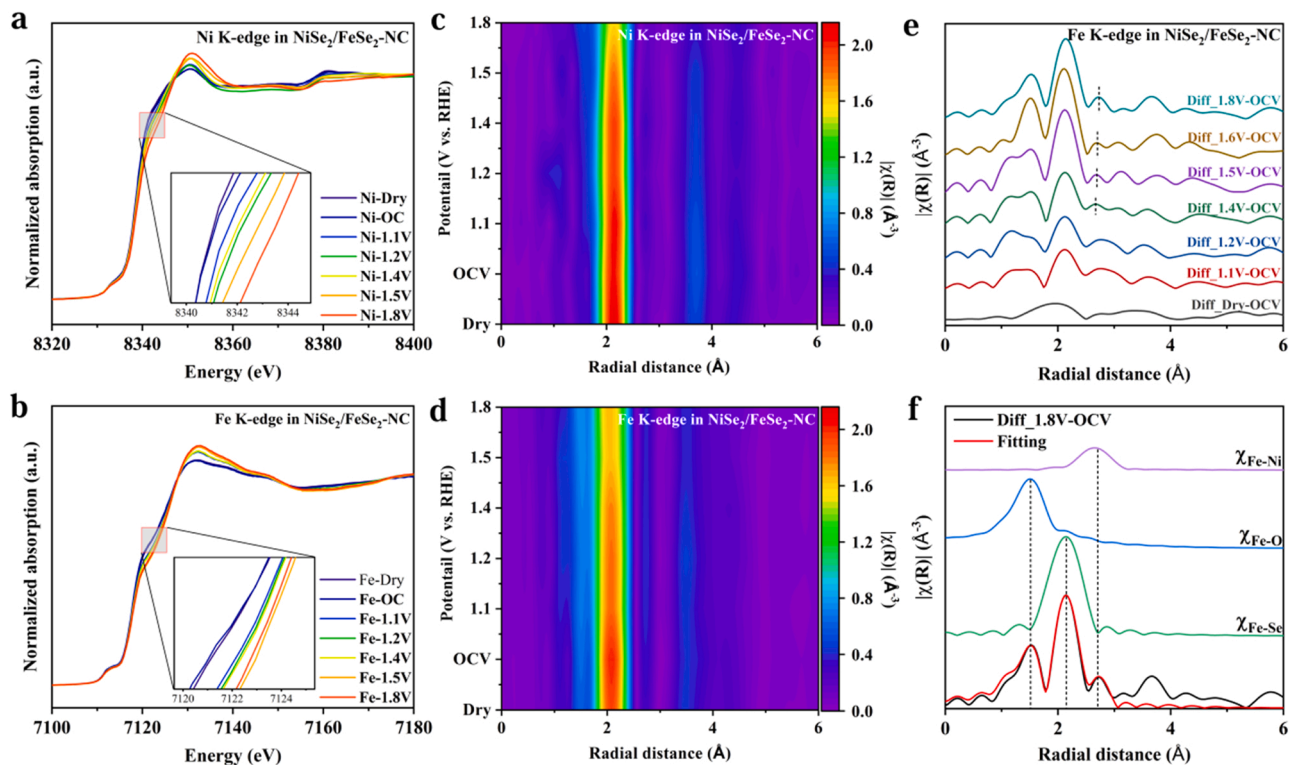


Fig. 5. Operando XAFS of NiSe₂/FeSe₂-NC under OER condition. (a, b) The evolution of Ni and Fe K-edge XANES and (c, d) the corresponding FT-EXAFS mappings under applied potentials. (e) Fourier transformed of k^2 -weighted diff-EXAFS of Fe K-edge. (f) Fitting result of diff-1.8 V-OCV. Contributions from different paths are shown separately.

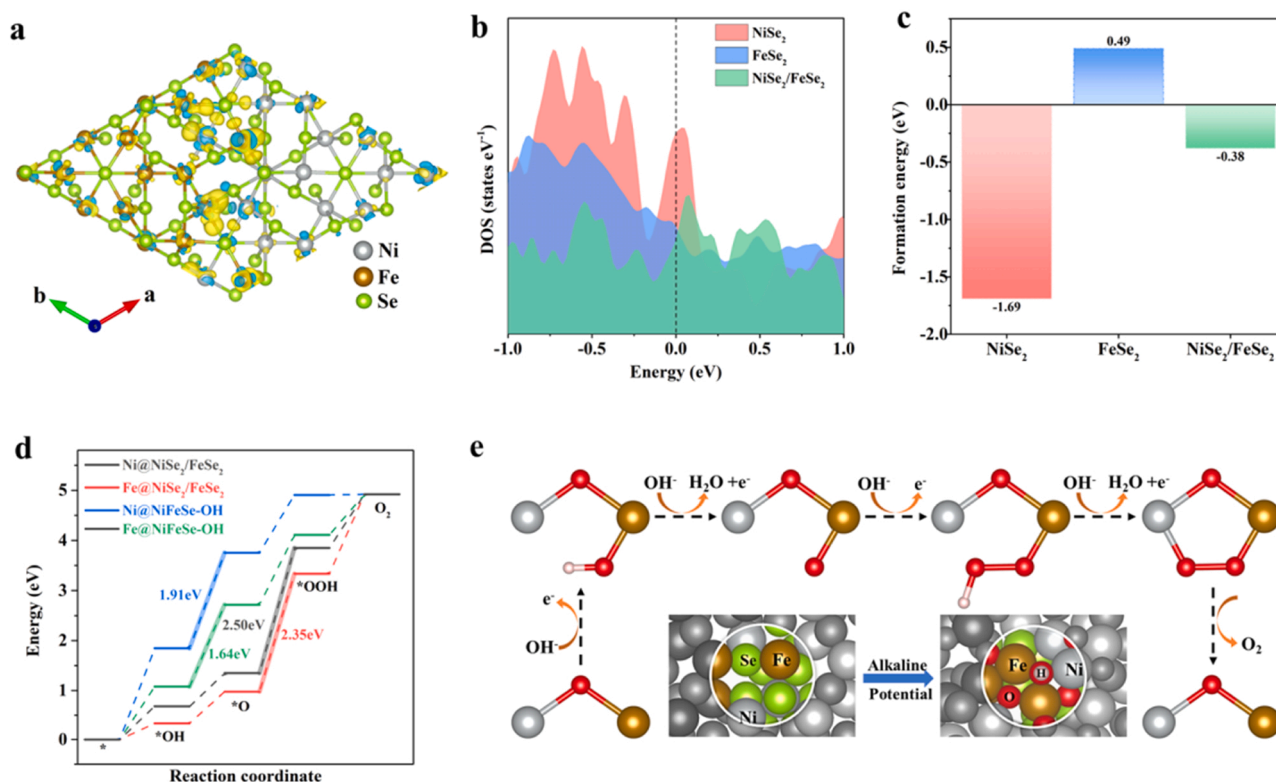


Fig. 6. Density functional theory (DFT) calculations. (a) Differential charge density between NiSe₂ and FeSe₂ in NiSe₂/FeSe₂. Yellow and green contours represent the charge accumulation and depletion, respectively. (b) Density of states of NiSe₂ and FeSe₂ and NiSe₂/FeSe₂. (c) Formation energy of Se vacancy in NiSe₂ and FeSe₂ and NiSe₂/FeSe₂. (d) Free energy diagram for OER of Fe and Ni sites on the surface of pristine and oxidized NiSe₂/FeSe₂ heterostructure. (e) The OER process for the NiSe₂/FeSe₂ heterostructure. Grey brown, green, white and pink balls represent Ni, Fe, Se, H and lattice O atoms, respectively. Red balls represent the O atoms in adsorbed intermediate.

activate Fe atoms into (oxy)hydroxide by reducing the Fe-Se bonding, as experimentally demonstrated by decreased Fe oxidation state and elongated Fe-Se bond length in comparison with FeSe₂, and also effectively alleviate the problem of complete dissolution of Se atoms such as in NiSe₂ to maintain the stability of main structure and keep high conductivity of Se compounds during the OER process. On the other hand, the activity of O-bridged Fe-Ni structure is also evaluated. Considering that the real active site of the catalyst is (oxy)hydroxide in the OER process, the free energy diagrams in the OER process were computed on Ni and Fe sites on the surface of pristine and oxidized NiSe₂/FeSe₂ heterostructure (Fig. 6d, Fig. S25 and S26), and four-step electron transfer mechanism was generally involved, including the adsorption oxygen-containing intermediates such as OH*, O* and OOH* in alkaline conditions [62,63]. The Ni^{III}-O-Fe^{III} structure effectively alleviates the adsorption of oxygen-containing intermediates, and decreases the overpotential of both Ni and Fe sites to 0.68 eV and 0.41 eV, respectively. Thus, the OER reaction kinetic process was promoted (Fig. 6e). In addition, the comparison of OER activity for the edge of Ni(OH)₂, Fe(OH)₂ and Ni-Fe(OH)₂ pristine and oxidized NiSe₂/FeSe₂ also reflects that Ni^{III}-O-Fe^{III} structure can effectively reduce the overpotential (Fig. S27 – S29), which is consistent with the experimental result. Additionally, compared with Ni site in NiSe₂/FeSe₂-NC, the Fe site surface exhibits significantly lower energy for O-O* adsorption. For Ni site, the energy barrier of O-O* changed to the O₂ desorption has much lower than Fe site, which is consistent with our experimental results. The above results together strongly confirm that the post-formed Ni^{III}-O-Fe^{III} structure serve as the real active centers in NiSe₂/FeSe₂-NC catalysts. FeSe₂ nanodomains for adsorbing OH* and generating O-O* intermediate, while the NiSe₂ component can catalyze O-O* and accelerate the formation of O₂.

4. Conclusions

In summary, we have conducted a systematic and deep investigation of the electronic structure and intrinsic OER activities of metal selenide compound catalysts. The heterostructural NiSe₂/FeSe₂-NC exhibits evidently enhanced performance compared to the individual NiSe₂-NC and FeSe₂-NC catalysts. Based on *In-situ/operando* Raman spectroscopy and X-ray absorption spectroscopy results and DFT calculations, it is identified that both Ni and Fe atoms are active catalytic sites. The high-valence Ni^{III}-O-Fe^{III} moieties, which are derived from surface reconstruction of NiSe₂/FeSe₂, act as the activity centers for OER. Specifically, Fe is the adsorption site for OH⁻ and catalyzes the O-O* intermediate formation; Ni is the converting site which transforms the O-O* intermediate to O₂ product. Hence, a strong synergistic effect between Ni and Fe sites in promoting the OER performance exists in the heterostructure. This work provides a deeper understanding of the intrinsic activity of heterostructured catalyst materials and thus may pave a way for designing high-performance bimetallic OER catalysts.

CCRediT authorship contribution statement

Shi Tao: Preparation, Investigation, Writing – original draft, Formal analysis, Visualization. **Guikai Zhang:** Preparation, Investigation. **Bin Qian:** Methodology, Investigation. **Jun Yang:** Methodology, Investigation. **Shengqi Chu:** Conceptualization, Investigation, Project administration, Funding acquisition, Supervision. **Chencheng Sun:** Conceptualization, Investigation. **Dajun Wu:** Conceptualization, Investigation. **Chencheng Sun:** Conceptualization, Investigation. Visualization, Project administration, Funding acquisition. **Li Song:** Formal analysis, Supervision, Writing – review & editing.

Declaration of Competing Interest

The authors declare no competing financial interest.

Data Availability

Data will be made available on request.

Acknowledgements

This work was financially supported in part by National Key Research and Development Program of China (2020YFA0405800) and the National Natural Science Foundation of China (Grant No. U1932201). We sincerely acknowledge the staff of the XAS beamlines of the Beijing Synchrotron Radiation Facility.

Appendix A. Supporting information

Supplementary data associated with this article can be found in the online version at doi:10.1016/j.apcatb.2023.122600.

References

- [1] N.T. Suen, S.F. Hung, Q. Quan, N. Zhang, Y.J. Xu, H.M. Chen, Electrocatalysis for the oxygen evolution reaction: recent development and future perspectives, *Chem. Soc. Rev.* 46 (2017) 337–365.
- [2] Q.R. Shi, C.Z. Zhu, D. Du, Y.H. Lin, Robust noble metal-based electrocatalysts for oxygen evolution reaction, *Chem. Soc. Rev.* 48 (2019) 3181–3192.
- [3] N.C.S. Selvam, L. Du, B.Y. Xia, P.J. Yoo, B. You, Reconstructed water oxidation electrocatalysts: the impact of surface dynamics on intrinsic activities, *Adv. Funct. Mater.* 31 (2020) 2008190.
- [4] C.X. Zhao, J.N. Liu, J. Wang, D. Ren, B.Q. Li, Q. Zhang, Recent advances of noble-metal-free bifunctional oxygen reduction and evolution electrocatalysts, *Chem. Soc. Rev.* 20 (2021) 7745–7778.
- [5] L.G. Li, P.T. Wang, Q. Shao, X.Q. Huang, Recent progress in advanced electrocatalyst design for acidic oxygen evolution reaction, *Adv. Mater.* 33 (2021) 2004243.
- [6] M.Q. Yu, E. Budiyo, H. Tuysuz, Principles of water electrolysis and recent progress in cobalt-, nickel-, and iron-based oxides for the oxygen evolution reaction, *Angew. Chem. Int. Ed.* 61 (2021), 202103824.
- [7] K.X. Wang, X.Y. Wang, Z.J. Li, B. Yang, M. Ling, X. Gao, J.G. Lu, Q.R. Shi, L.C. Lei, G. Wu, Y. Hou, Designing 3d dual transition metal electrocatalysts for oxygen evolution reaction in alkaline electrolyte: beyond oxides, *Nano Energy* 77 (2020), 105162.
- [8] M. Wang, L. Zhang, Y.J. He, H.W. Zhu, Recent advances in transition-metal-sulfide-based bifunctional electrocatalysts for overall water splitting, *J. Mater. Chem. A* 9 (2021) 5320–5363.
- [9] S. Lee, K. Banjac, M. Lingenfelder, X.L. Hu, Oxygen isotope labelling experiments reveal different reaction sites for the oxygen evolution reaction on nickel and nickel iron oxides, *Angew. Chem. Int. Ed.* 58 (2019) 10295–10299.
- [10] Z.F. Huang, J.J. Song, Y.H. Du, S.B. Xi, S. Dou, J.M.V. Nsanzimana, C. Wang, Z. C. Xu, X. Wang, Chemical and structural origin of lattice oxygen oxidation in Co-Zn oxyhydroxide oxygen evolution electrocatalysts, *Nat. Energy* 4 (2019) 329–338.
- [11] X. Peng, Y.J. Yan, X. Jin, C. Huang, W.H. Jin, B. Gao, P.K. Chu, Recent advance and perspectives of electrocatalysts based on transition metal selenides for efficient water splitting, *Nano Energy* 78 (2020), 105234.
- [12] G. Fang, Q. Wang, J. Zhou, Y. Lei, Z. Chen, Z. Wang, A. Pan, S. Liang, Metal organic framework-templated synthesis of bimetallic selenides with rich phase boundaries for sodium-ion storage and oxygen evolution reaction, *ACS Nano* 13 (2019) 5635–5645.
- [13] J.X. Kang, X.Y. Qiu, Q. Hu, J. Zhong, X. Gao, R. Huang, C.Z. Wan, L.M. Liu, X. F. Duan, L. Guo, Valence oscillation and dynamic active sites in monolayer NiCo hydroxides for water oxidation, *Nat. Catal.* 4 (2021) 1050–1058.
- [14] S. Ibraheem, S.G. Chen, L.L. Peng, J. Li, L. Li, Q. Liao, M.H. Shao, Z.D. Wei, Strongly coupled iron selenides-nitrogen-bond as an electronic transport bridge for enhanced synergistic oxygen electrocatalysis in rechargeable zinc-O₂ batteries, *Appl. Catal. B-Environ.* 265 (2020), 118569.
- [15] W.R. Cheng, X. Zhao, H. Su, F.M. Tang, W. Che, H. Zhang, Q.H. Liu, Lattice-strained metal-organic-framework arrays for bifunctional oxygen electrocatalysis, *Nat. Energy* 4 (2019) 115–122.
- [16] X.Y. Zhang, B.Y. Guo, X.Y. Chen, L. Zhao, B. Dong, M. Yang, J.F. Yu, L. Wang, C. G. Liu, Y.M. Chai, Template confined strategy for constructing nickel cobalt selenide nanoarrays for efficient oxygen evolution reaction, *Mater. Today, Energy* 17 (2020), 100468.
- [17] P.K. Wei, Z.W. Hao, Y. Yang, M.Y. Liu, H.J. Zhang, M.R. Gao, S.H. Yu, Unconventional dual-vacancies in nickel diselenide-graphene nanocomposite for high-efficiency oxygen evolution catalysis, *Nano Res.* 13 (2020) 3292–3298.
- [18] X. Zhao, X.Q. Li, Y. Yan, Y.L. Xing, S.C. Lu, L.Y. Zhao, S.M. Zhou, Z.M. Peng, J. Zeng, Electrical and structural engineering of cobalt selenide nanosheets by Mn modulation for efficient oxygen evolution, *Appl. Catal. B-Environ.* 236 (2018) 569–575.
- [19] Z.W. Fang, L.L. Peng, H.F. Lv, Y. Zhu, C.S. Yan, S.Q. Wang, P. Kalyani, X.J. Wu, G. H. Yu, Metallic transition metal selenide holey nanosheets for efficient oxygen evolution electrocatalysis, *ACS Nano* 11 (2017) 9550–9557.

- [20] X.R. Zheng, J.F. Zhang, J.H. Wang, Z.J. Zhang, W.B. Hu, Y.J. Han, Facile synthesis of nickel cobalt selenide hollow nanospheres as efficient bifunctional electrocatalyst for rechargeable Zn-air battery, *Sci. China Mater.* 63 (2020) 347–355.
- [21] M. Luo, W. Sun, B.B. Xu, H. Pan, Y. Jiang, Interface engineering of air electrocatalysts for rechargeable zinc-air batteries, *Adv. Energy Mater.* 11 (2021) 2002762.
- [22] Q.C. Xu, J.H. Zhang, H.X. Zhang, L.Y. Zhang, L. Chen, Y.J. Hu, H. Jiang, C.Z. Li, Atomic heterointerface engineering overcomes the activity limitation of electrocatalysts and promises highly-efficient alkaline water, *Energy Environ. Sci.* 14 (2021) 5228–5259.
- [23] H. Ding, H.F. Liu, W.S. Chu, C.Z. Wu, Y. Xie, Structural transformation of heterogeneous materials for electrocatalytic oxygen evolution reaction, *Chem. Rev.* 121 (2021) 13174–13212.
- [24] P.L. Zhai, Y.X. Zhang, Y.Z. Wu, J.F. Gao, B. Zhang, S.Y. Cao, Y.T. Zhang, Z.W. Li, L. C. Sun, G. Hou, Engineering active sites on hierarchical transition bimetal oxides/sulfides heterostructure array enabling robust overall water splitting, *Nat. Commun.* 11 (2020) 5462.
- [25] J.W. Nai, X.Z. Xu, Q.F. Xie, G.X. Lu, Y. Wang, D.Y. Luan, X.Y. Tao, X.W. Lou, Construction of Ni(CN)₂/NiSe₂ heterostructures by stepwise topochemical pathways for efficient electrocatalytic oxygen evolution, *Adv. Mater.* 34 (2022) 2104405.
- [26] X.R. Zheng, X.P. Han, Y.H. Cao, Y. Zhang, D. Nordlund, J.H. Wang, S.L. Chou, H. Liu, L.L. Li, C. Zhong, Y.D. Deng, W.B. Hu, Identifying dense NiSe₂/CoSe₂ heterointerfaces coupled with surface high-valence bimetallic sites for synergistically enhanced oxygen electrocatalysis, *Adv. Mater.* 32 (2020) 2000607.
- [27] F. Song, L.C. Bai, A. Moysiadou, S. Lee, C. Hu, L. Liardet, X.L. Hu, Transition metal oxide as electrocatalysts for the oxygen evolution reaction in alkaline solutions: an application-inspired renaissance, *J. Am. Chem. Soc.* 140 (2018) 7748–7759.
- [28] M.L. Yuan, S. Dipazir, M. Wang, Y. Sun, D.L. Gao, Y.L. Bai, M. Zhang, P.L. Lu, H. Y. He, X.Y. Zhu, S.W. Li, Z.J. Liu, Z.P. Luo, G.J. Zhang, Polyoxometalate-assisted formation of CoSe/MoSe₂ heterostructures with enhanced oxygen evolution activity, *J. Mater. Chem. A* 7 (2019) 3317–3326.
- [29] W. Li, Y.L. Niu, X.J. Wu, F.W. Wu, T.H. Li, W.H. Hu, Heterostructured CoSe₂/FeSe₂ nanoparticles with abundant vacancies and strong electronic coupling supported on carbon nanorods for oxygen evolution electrocatalysis, *ACS Sustain. Chem. Eng.* 8 (2020) 4658–4666.
- [30] C.Y. Xu, Q.H. Li, J.L. Shen, Z. Yuan, J.Q. Ning, Y.J. Zhong, Z.Y. Zhang, Y. Hu, Facile sequential ion exchange strategy to synthesize CoSe₂/FeSe₂ double-shelled hollow nanocuboids for highly active and stable oxygen evolution reaction, *Nanoscale* 11 (2019) 10738–10745.
- [31] S.W. Zuo, Z.P. Wu, H.B. Zhang, X.W. Lou, Operando monitoring and deciphering the structural evolution in oxygen evolution electrocatalysis, *Adv. Energy Mater.* 12 (2022) 2103383.
- [32] Y.P. Zhu, T.R. Kuo, Y.H. Li, M.Y. Qi, G. Chen, J.L. Wang, Y.J. Xu, H.M. Chen, Emerging dynamic structure of electrocatalysts unveiled by in situ X-ray diffraction/absorption spectroscopy, *Energy Environ. Sci.* 14 (2021) 1928–1958.
- [33] Y. Yang, Y.K. Kang, H.H. Zhao, X.P. Dai, M.L. Cui, X.B. Luan, X. Zhang, F. Nie, Z. T. Ren, W.Y. Song, An interfacial electron transfer on tetrahedral NiS₂/NiSe₂ heterocages with dual-phase synergy for efficiently triggering the oxygen evolution reaction, *Small* 16 (2019) 1905083.
- [34] S.K. Jiang, M.J. Xiang, J.Y. Zhang, S.Q. Chu, A. Marcelli, W.S. Chu, D.J. Wu, B. Qian, S. Tao, L. Song, Rational design of hierarchical FeSe₂ encapsulated with bifunctional carbon cuboids as an advanced anode for sodium-ion batteries, *Nanoscale* 12 (2020) 22210–22216.
- [35] G. Kresse, J. Furthmüller, Efficiency of ab-initio total energy calculations for metals and semiconductors using a plane-wave basis set, *Comp. Mater. Sci.* 6 (1996) 15–50.
- [36] P.E. Blochl, Projector augmented-wave method, *Phys. Rev. B Condens. Matter* 50 (1994) 17953–17979.
- [37] K.B. John, P. Perdew, Matthias Ernzerhof, Generalized gradient approximation made simple, *Phys. Rev. Lett.* 77 (1996) 3865–3868.
- [38] J. Zhang, T. Wang, D. Pohl, B. Rellinghaus, R. Dong, S.H. Liu, X.D. Zhuang, X. L. Peng, Interface engineering of MoS₂/NiS₂ heterostructures for highly enhanced electrochemical overall-water-splitting activity, *Angew. Chem. Int. Ed.* 55 (2016) 6702–6707.
- [39] N. Zhang, Y. Hu, L. An, Q. Li, J. Yin, J.Y. Li, R. Yang, M. Lu, S. Zhang, P.X. Xi, C. H. Yan, Surface activation and Ni-S stabilization in NiO/NiS₂ for efficient oxygen evolution reaction, *Angew. Chem. Int. Ed.* 61 (2022), e202207217.
- [40] X. Bo, R.K. Hocking, S. Zhou, Y.B. Li, X.J. Chen, J.C. Zhuang, Y. Du, C. Zhao, Capturing the active sites of multimetallic (Oxy)hydroxides for oxygen evolution reactions, *Energy Environ. Sci.* 13 (2020) 4225–4237.
- [41] C.C. Liu, Y. Han, L.B. Yao, L.M. Liang, J.Y. He, Q.Y. Hao, J. Zhang, Y. Li, H. Liu, Engineering bimetallic NiFe-based hydroxides/selenides heterostructure nanosheet arrays for highly-efficient oxygen evolution reaction, *Small* 17 (2021) 2007334.
- [42] Z.D. Huang, C. Feng, J.P. Sun, B. Xu, T.X. Huang, X.K. Wang, Nanosheets-derived yolk-shell Ni_{0.85}Se@NC with rich Se-vacancies for enhanced water electrolysis, *CCS Chem.* 2 (2020) 2696–2711.
- [43] X. Xu, H.F. Liang, F.W. Ming, Z.B. Qi, Y.Q. Xie, Z.C. Wang, Prussian blue analogues derived penroseite (Ni, Co)Se₂ nanocages anchored on 3D graphene aerogel for efficient water splitting, *ACS Catal.* 7 (2017) 6394–6399.
- [44] L. Lv, Z.S. Li, K.H. Xue, Y.J. Ruan, X. Ao, H.Z. Wan, X.S. Miao, B.S. Zhang, J. J. Jiang, C.D. Wang, K. Ostrikov, Tailoring the electrocatalytic activity of bimetallic nickel-iron diselenide hollow nanochains for water oxidation, *Nano Energy* 47 (2018) 275–284.
- [45] L. Zhang, C.J. Lu, Y. Fei, R.L.J. Pang, Y. Liu, Z.Y. Wu, Z.P. Shao, Z.M. Sun, L.F. Hu, Selenic Acid etching assisted vacancy engineering for designing highly active electrocatalysts toward the oxygen evolution reaction, *Adv. Mater.* 33 (2021) 2007523.
- [46] Y.Q. Zhao, B. Jin, Y. Zheng, H.Y. Jin, Y. Jiao, S.Z. Qiao, Charge state manipulation of cobalt selenide catalyst for overall seawater electrolysis, *Adv. Energy Mater.* 8 (2018) 1801926.
- [47] H.L. Zhu, R. Jiang, X.Q. Chen, Y.G. Chen, L.Y. Wang, 3D nickel-cobalt diselenide nanonetwork for highly efficient oxygen evolution, *Sci. Bull.* 62 (2017) 1373–1379.
- [48] J.W. Nai, Y. Lu, L. Yu, X. Wang, X.W. Lou, Formation of Ni-Fe mixed diselenide nanocages as a superior oxygen evolution electrocatalyst, *Adv. Mater.* 29 (2017) 1703870.
- [49] Y.G. Zhao, N.C. Dongfang, C.A. Triana, C. Huang, R. Erni, W.C. Wan, J.G. Li, D. Stoian, L. Pan, P. Zhang, J.G. Lan, M. Iannuzzi, G.R. Patzke, Dynamics and control of active sites in hierarchically nanostructured cobalt phosphide/chalcogenide-based electrocatalysts for water splitting, *Energy Environ. Sci.* 15 (2021) 727–739.
- [50] Z.W. Gao, J.Y. Liu, X.M. Chen, X.L. Zheng, J. Mao, H. Liu, T. Ma, L. Li, W.C. Wang, X.W. Du, Engineering NiO/NiFe LDH intersection to bypass scaling relationship for oxygen evolution reaction via dynamic tridimensional adsorption of intermediates, *Adv. Mater.* 31 (2019) 1804769.
- [51] X.L. Zheng, B. Zhang, P.D. Luna, Y.F. Liang, R. Comin, O. Voznyy, L.L. Han, F. P. García de Arquer, M. Liu, G.T. Dinh, T. Regier, J.J. Dynes, S.S. He, H.L. Xin, H. S. Peng, D. Prendergast, X.W. Du, E.H. Sargent, Theory-driven design of high-valence metal sites for water oxidation confirmed using in situ soft X-ray absorption, *Nat. Chem.* 10 (2018) 149–154.
- [52] W.H. Choi, K.H. Kim, H. Lee, J.W. Choi, D.G. Park, G.H. Kim, K.M. Choi, J.K. Kang, Metal-organic fragments with adhesive excipient and their utilization to stabilize multimetallic electrocatalysts for high activity and robust durability in oxygen evolution reaction, *Adv. Sci.* 8 (2021), 100044.
- [53] X.Z. Su, Y. Wang, J. Zhou, S.Q. Gu, J. Li, S. Zhang, Operando spectroscopic identification of active sites in NiFe Prussian blue analogues as electrocatalysts: activation of oxygen atoms for oxygen evolution reaction, *J. Am. Chem. Soc.* 140 (2018) 11286–11292.
- [54] M. Yoshida, Y. Mitsutomi, T. Mineo, M. Nagasaka, H. Yuzawa, N. Kosugi, H. Kondoh, Direct observation of active nickel oxide cluster in nickel–borate electrocatalyst for water oxidation by in situ O K-edge X-ray absorption spectroscopy, *J. Phys. Chem. C* 119 (2015) 11279–11286.
- [55] Y.J. Wu, J. Yang, T.X. Tu, W.Q. Li, P.F. Zhang, Y. Zhou, J.F. Li, J.T. Li, S.G. Sun, Evolution of cationic vacancy defects: a motif for surface restructuring of OER precatalyst, *Angew. Chem. Int. Ed.* 60 (2021) 22470–22474.
- [56] Y.M. Shi, W. Du, W. Zhou, C.H. Wang, S.S. Lu, S.Y. Lu, B. Zhang, Unveiling the promotion of surface-adsorbed chalcogenate on the electrocatalytic oxygen evolution reaction, *Angew. Chem. Int. Ed.* 59 (2020) 22470–22474.
- [57] S. Lee, K. Banjac, M. Lingenfelder, X.L. Hu, Oxygen isotope labelling experiments reveal different reaction sites for the oxygen evolution reaction on nickel and nickel iron oxides, *Angew. Chem. Int. Ed.* 58 (2019) 10295–10299.
- [58] C.J. Hu, Y.F. Hu, C.H. Fan, L. Yang, Y.T. Zhang, H.X. Li, W. Xie, Surface-enhanced Raman spectroscopic evidences of key intermediate species and role of NiFe dual-catalytic center in water oxidation, *Angew. Chem. Int. Ed.* 60 (2021) 19774–19778.
- [59] Y.C. Zheng, G.K. Zhang, P.J. Zhang, S.Q. Chu, D.J. Wu, C.C. Sun, B. Qian, S. M. Chen, S. Tao, L. Song, Structural investigation of metallic Ni nanoparticles with N-doped carbon for efficient oxygen evolution reaction, *Chem. Eng. J.* 429 (2022), 132122.
- [60] C.F. Li, L.J. Xie, J.W. Zhao, L.F. Gu, H.B. Tang, L.R. Zheng, G.R. Li, Interfacial Fe–O–Ni–O–Fe bonding regulates the active Ni sites of Ni-MOFs via iron doping and decorating with FeOOH for super-efficient oxygen evolution, *Angew. Chem. Int. Ed.* 61 (2022), e202116934.
- [61] Y. Wang, X.P. Li, M.M. Zhang, Y.G. Zhou, D.W. Rao, C. Zhong, J.F. Zhang, X. P. Han, W.B. Hu, Y.C. Zhang, K. Zaghib, Y.S. Wang, Y.D. Deng, Lattice-strain engineering of a homogeneous NiS_{0.5}Se_{0.5} core-shell nanostructure as a highly efficient and robust electrocatalyst for overall water splitting, *Adv. Mater.* 32 (2020) 2000231.
- [62] L.Y. Hu, X. Zeng, X.Q. Wei, H.J. Wang, Y. Wu, W.L. Gu, L. Shi, C.Z. Zhu, Interface engineering for enhancing electrocatalytic oxygen evolution of NiFe LDH/NiTe heterostructures, *Appl. Catal. B-Environ.* 273 (2020), 119014.
- [63] Z.P. Wu, H.B. Zhang, S.W. Zuo, Y. Wang, S.L. Zhang, J. Zhang, S.Q. Zang, X.W. Lou, Manipulating the local coordination and electronic structures for efficient electrocatalytic oxygen evolution, *Adv. Mater.* 33 (2021) 2103004.